Research in Astronomy and Astrophysics, 24:035001 (9pp), 2024 March https://doi.org/10.1088/1674-4527/ad1f43

Study of Type-B QPOs Observed in Black Hole X-Ray Binary Swift J1728.9-3613

Raj Kumar
Astrophysical Sciences Division, Bhabha Atomic Research Centre, Mumbai 400085, India; arya95raj@gmail.com
Homi Bhabha National Institute, Mumbai 400094, India
Received 2023 August 10; revised 2023 December 24; accepted 2024 January 15; published 2024 February 20

Abstract

We report the detection of type-B quasi-periodic oscillation (QPO) of the black hole X-ray binary Swift J1728.9-3613 observed by NICER during the 2019 outburst. A type-B QPO was observed for the first two days and it disappeared as flux increased, but again appeared at ∼7.70 Hz when flux was dramatically decreased. The source was found in the soft intermediate state during these observations. We further studied the energy dependence of the QPO. We found that QPO was observed only for a higher energy range implying that the origin of QPO is possibly due to the corona emitting higher energy photons by the inverse Compton process. The variation of spectral parameters can be explained with the disk truncation model. The fractional rms was found to be monotonically increased with energy. The phase lag spectrum followed the "U-shaped" curve. The rms and phase lag spectrum are modeled and explained with the single-component Comptonization model `vkompthdk`.

Key words: X-rays: binaries – accretion – accretion disks – X-rays: individual: (Swift J1728.9-3613)

1. Introduction

Accretion disks, formed around black hole X-ray binaries (BHXRBs) due to Roche lobe overflow or wind-fed accretion from a companion star to the black hole (BH), emit strong electromagnetic radiation in X-rays. BHXRBs are observed in two classes- (i) persistent X-ray sources and (ii) transient X-ray sources. Persistent sources are always observed in the bright phase. On the other hand, transient sources are observed in a bright phase known as an outburst, and then they go into a quiescent state for a long time, from months to decades. Based on the thermal emission and Comptonized component, a BH transient evolves through different spectral states like low/hard state (LHS), high/soft state (HSS), hard intermediate state (HIMS) and soft intermediate state (SIMS) during its outburst (Homan & Belloni 2005). LHS is dominated by a Comptonized component with a photon index ∼1.7 and peak emission at ∼60–100 keV (Joinet et al. 2008; Motta et al. 2009; Gilfanov 2010). In the LHS, soft photons originating from the accretion disk are scattered by thermal electrons in the Comptonization region. HSS is thermally dominated with disk temperature ∼0.5–1 keV (Remillard & McClintock 2006) and a high energy tail can be produced by the scattering of soft photons by hybrid, thermal/nonthermal electrons (Zdziarski & Gierliński 2004). Intermediate states are found between LHS and HSS but in general, HIMS is slightly harder than SIMS (Belloni et al. 2011).

As spectral behavior changes with the evolution during an outburst, the timing properties also change for BH transients (Belloni et al. 2011). The power density spectrum (PDS) is the most useful tool to probe the variability of X-ray binaries (Belloni et al. 2005; Belloni 2010; De Marco et al. 2022). In the study of XRBs, narrow peaks known as quasi-periodic oscillations (QPOs) are commonly observed in the X-ray PDS. QPOs are thought to originate from inner accretion flow but their exact origin is still debatable (Motta et al. 2011). The low-frequency QPOs (LFQPOs) are classified into three categories: type-A, B and C. Type-A QPOs are generally observed with a very weak, flat and broad peak in the soft state in the frequency range of about 6–8 Hz (Homan & Belloni 2005). Type-B QPOs are observed in a narrow frequency range of 4–8 Hz with a weak read noise in PDS and fractional root mean square (rms) variability of ∼5% during SIMS (Casella et al. 2005; Belloni & Motta 2016). Type-C QPOs are mostly observed during LHS and HIMS, with a frequency range of 0.1–30 Hz with a flat top noise in PDS. Around 30% fractional rms variability of Type-C QPOs has been observed in LHS, which decreases to ∼10% in HIMS (Wijnands & van der Klis 1999; Casella et al. 2005; Motta 2016).

Swift J1728.9-3613 is a newly detected X-ray transient discovered by the Burst Alert Telescope (BAT) onboard the SWIFT observatory (Barthelmy et al. 2019). Saha et al. (2023) studied the timing and spectral properties of Swift J1728.9-3613, identified it as a BHXRB , and put a lower limit on the BH mass of ∼4.6 solar mass. Balakrishnan et al. (2023) concluded that the BH in this system is likely associated with the supernova remnant G351.9-0.9. Draghis et al. (2023) measured the spin of the BH to be ∼0.86 using the relativistic

Table 1
Details of NICER Observations used in this Work

Obs ID	Start Time (MJD)	Stop Time (MJD)	Average Count Rate NICER (1–10 keV)	QPO
1200550101	58512.64	58512.97	560	yes
1200550102	58513.02	58513.68	666	yes
1200550102	58513.72	58514.00	1128	no
1200550103	58514.03	58514.26	1316	no
1200550103	58514.36	58514.90	990	yes

reflection method and also measured the small inclination angle of the accretion disk $i < 10^{\circ}$. Heiland et al. (2023) suggest that the viscous inflow timescale of matter in the standard disk is responsible for the observed continuum lag of 8.4 ± 1.9 days between soft energy band (2–4) keV and hard energy band (10–20) keV. Heiland et al. (2023) also estimated the spin parameter of ∼0.6–0.7 with an inclination angle of ∼45°–70° using spectral analysis of NuSTAR data.

NICER observed this source when it reached the SIMS, where type-B QPO was observed when observation of the source started (Enoto et al. 2019). In our work, we mainly focus on the study of Type-B QPO observed in Swift J1728.9-3613. Observation details are tabulated in Table 1. Observations and data analysis are discussed in Section 2. The results of our study are presented and discussed in Section 3. We conclude our results in Section 4.

2. Observations and Data Analysis

NICER is a payload on the International Space Station (ISS). It has an X-ray timing instrument (XTI) that operates in the soft X-ray energy range (0.2–12 keV) (Gendreau et al. 2016). XTI is a collection of 56 X-ray concentrator optics with silicon drift detectors. Out of 56 detectors, 52 detectors are active at present. Here, we used 50 detectors for our analysis and discarded Focal Plane Modules (FPMs) 34 and 14 using the "detlist' flag because they are noisy under certain conditions. NICER observed Swift J1728.9-3613 during the 2019 outburst. We mainly considered those observations which lie in SIMS. Details of the observation used in our work are tabulated in Table 1. We employed `HEASOFT-6.31.1` and `NICERDAS` $2022-12-16\_V010a$ for the analysis of the data. The NICER CALDB version of 20221001 was utilized while extracting the level 2 data from level 1 data. A lightcurve was generated using the "nicerl3-lc" pipeline with time bin 1 and 0.01 s. We relied on the "nicerl3-spec" pipeline to extract spectrum, arf, rmf and background files. We added a 1% systematic error to the data and grouped each spectrum with at least 25 counts for each bin using the grppha task. We extracted the background for the `SCORPEON` model.

Saha et al. (2023) identified Swift J1728.9-3613 as a BHXRB. They studied the evolution of outburst using a hardness-intensity diagram (HID) and found that Swift J1728.9-3613 stayed in SIMS for ∼22 days. The HID of Swift J1728.9-3613 is shown in Figure 1. The observations considered in this work are indicated by red points on HID. These observations belong to the SIMS as found by Enoto et al. (2019); Saha et al. (2023). The upper panel of Figure 2 displays the 1–10 keV NICER lightcurve of Swift J1728.9-3613 from Modified Julian Date (MJD) 58512.6 to 58515.2 with bin size 60 s. We divided the lightcurve into 5-segments. The count rate slowly increased from seg-1 to seg-4. Then count rate rapidly decreased by 25% in seg-5. The average count rate in seg-5 reached 990 counts/sec from 1316 counts/sec in seg-4. We computed the hardness ratio (HR) by taking the ratio of the count rate in the energy range 4–10 keV and 1–3 keV. The HR increased in seg-3 and seg-4. Then it again decreased in seg-5. The HR is plotted in the lower panel of Figure 2.

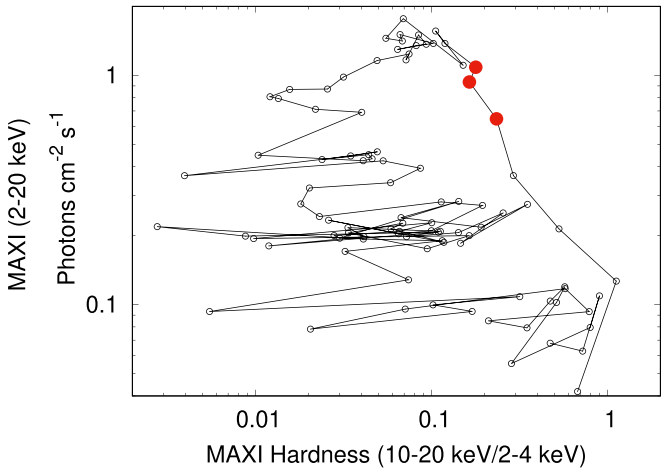

Figure 1. HID of Swift J1728.9-3613 during the 2019 outburst using MAXI/GSC. The HR was obtained from 2–4 keV and 10–20 keV photon flux. The red points indicate the NICER observations analyzed in this work.

3. Results and Discussions

3.1. Timing Analysis

We extracted the lightcurve in the energy range 1–10 keV with a time resolution of 0.01 s for each segment. Then we used the "powspec" tool to calculate the power spectrum for an interval length of 10.24 s with Miyamoto normalization (Miyamoto et al. 1991). It corresponds to Nyquist frequency 50 Hz and 1024 (2^{10}) bins per interval. The PDS was rebinned using the logarithmic binning factor of 1.05. The PDS was converted to an XSPEC readable file using the `ftflx2xsp` task. The PDS was then fitted with a combination of Lorentzians. The Lorentzian used in this work is given by,

$$P(\nu) = \frac{r^2\Delta}{2\pi}\frac{1}{[(\nu-\nu_0)^2 + (\Delta/2)^2]},$$

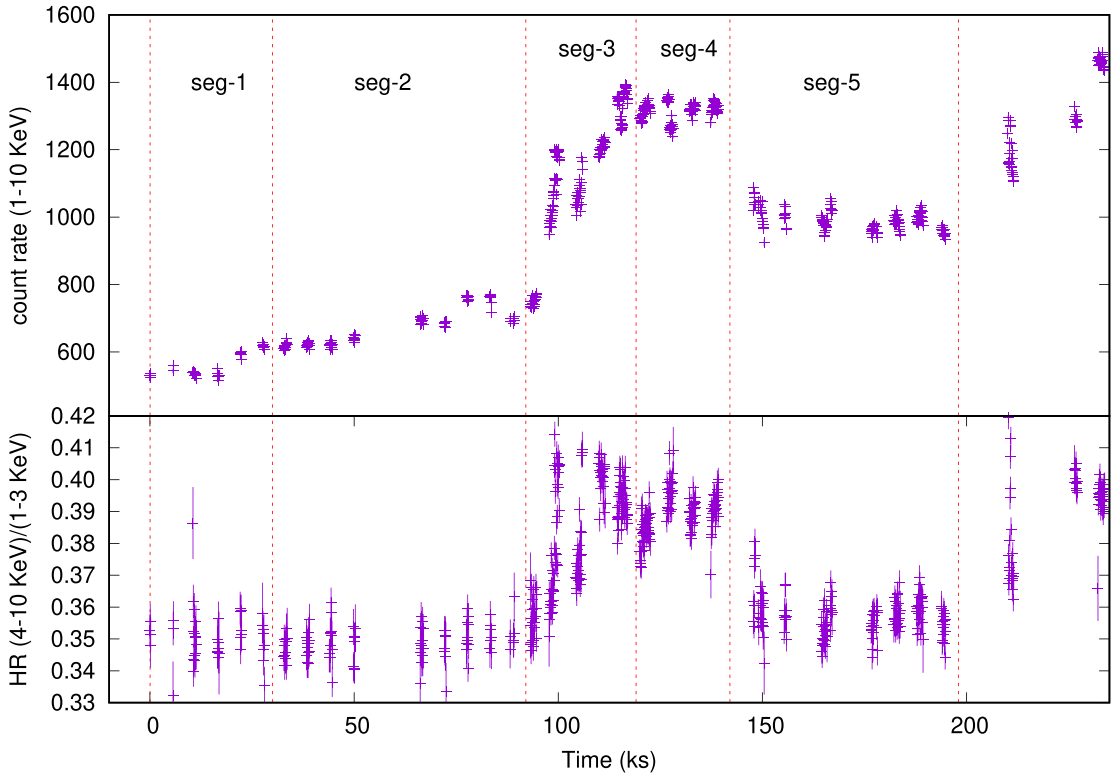

Figure 2. NICER lightcurve in 1–10 keV range and HR with bin size 60 s. HR is defined as the count rate ratio in 4–10 keV energy range to that in 1–3 keV energy range. Different segments are also shown in the figure.

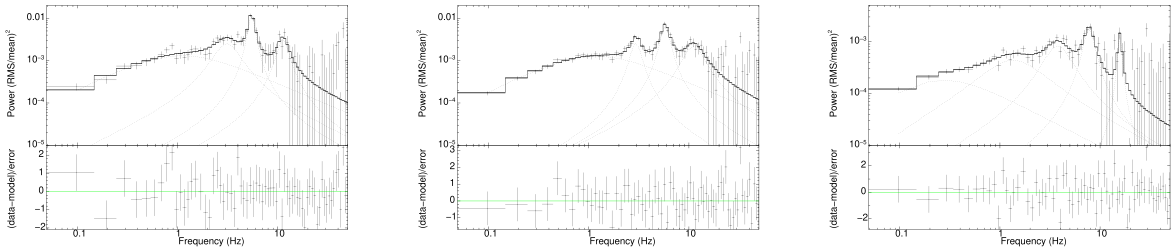

Figure 3. PDS of Seg-1 (left panel), Seg-2 (middle panel) and Seg-5 (right panel). Type-B QPO was observed during these segments. The PDS of Seg-1 and Seg-2 were fitted with one zero-frequency Lorentzian and three Lorentzians. The PDS of Seg-5 was fitted with one zero-frequency Lorentzian and four Lorentzians.

where ν_0 is the centroid frequency, Δ is the full width at half maximum (FWHM) and r is the integrated fractional rms (Belloni et al. 2002). In this definition, the quality factor Q is defined as $\sim\nu_0/\Delta$. The significance of QPO is calculated by dividing the norm of power by 1σ negative error. Q value greater than 3 indicates the presence of QPO. The power spectra of Seg-1 and Seg-2 are fitted with a combination of three Lorentzians and one zero-frequency Lorentzian, while Seg-3 is fitted with a combination of two Lorentzians and one zero-frequency Lorentzian. Seg-4 is Poisson noise-dominated and fitted only with a power law, while we require four Lorentzians and one zero-frequency Lorentzian to fit the power spectra of Seg-5.

The PDS for each segment fitted with Lorentzians is depicted in Figure 3. The details of fitted parameters are tabulated in Table 2. An LFQPO was observed in Seg-1 at $\sim$5.46 Hz with Q value $\sim$7.2 and rms $\sim$5.1% with a significance of $\sim 8\sigma$. A harmonic was also observed at $\sim$11.15 Hz with Q value $\sim$5.0 and rms $\sim$3.5%. The significance of the harmonic is $\sim 4\sigma$. An LFQPO was observed in Seg-2 at $\sim$5.76 Hz with Q value $\sim$5.0 and rms $\sim$4.5% with a significance of $\sim 10.8\sigma$. A subharmonic was also observed at $\sim$2.93 Hz with Q value $\sim$4.1 and rms $\sim$3.1%. The significance of the harmonic is $\sim 6.4\sigma$. An LFQPO was observed in Seg-5 at $\sim$7.7 Hz with Q value $\sim$4.2 and rms $\sim$2.5% with a significance of $\sim 6.6\sigma$. A subharmonic and

Table 2
Fit Parameters for Power Spectrum in Energy Range 1.0–10.0 keV

Model	Parameter	Seg-1	Seg-2	Seg-3	Seg-4	Seg-5
Lorentzian 1	ν (Hz)	0(f)	0(f)	0(f)	⋯	0(f)
	Δ (Hz)	$2.23^{+0.70}_{-0.54}$	$2.41^{+0.37}_{-0.31}$	$0.31^{+0.16}_{-0.18}$	—	$0.53^{+0.29}_{-0.30}$
	norm (10^{-3})	$4.08^{+0.95}_{-0.93}$	$3.93^{+0.40}_{-0.38}$	$0.33^{+0.09}_{-0.08}$	—	$0.58^{+0.25}_{-0.32}$
Lorentzian 2	ν (Hz)	$2.96^{+0.30}_{-0.24}$	$2.93^{+0.07}_{-0.08}$	⋯	⋯	$3.57^{+0.34}_{-0.36}$
	Δ (Hz)	$1.84^{+1.56}_{-0.75}$	$0.71^{+0.29}_{-0.23}$	⋯	⋯	$2.45^{+1.45}_{-0.99}$
	norm (10^{-3})	$2.17^{+0.14}_{-0.87}$	$0.99^{+0.28}_{-0.25}$	⋯	⋯	$0.78^{+0.40}_{-0.42}$
Lorentzian 3	ν (Hz)	$5.46^{+0.06}_{-0.06}$	$5.76^{+0.07}_{-0.07}$	$8.03^{+1.32}_{-0.86}$	⋯	$7.70^{+0.19}_{-0.20}$
	Δ (Hz)	$0.76^{+0.24}_{-0.22}$	$1.16^{+0.28}_{-0.24}$	$2.23^{+4.01}_{1.94}$	⋯	$1.84^{+0.73}_{-0.55}$
	norm (10^{-3})	$2.63^{+0.50}_{-0.57}$	$2.00^{+0.30}_{-0.31}$	$0.18^{+0.23}_{-0.14}$	⋯	$0.64^{+0.17}_{-0.16}$
Lorentzian 4	ν (Hz)	$11.15^{+0.72}_{-0.81}$	$10.83^{+0.78}_{-0.89}$	⋯	⋯	$15.73^{+0.39}_{-0.54}$
	Δ (Hz)	$2.23^{+2.11}_{-1.46}$	$5.14^{+3.74}_{-2.17}$	⋯	⋯	$1.15^{+1.90}_{-1.09}$
	norm (10^{-3})	$1.24^{+0.54}_{-0.47}$	$1.56^{+0.61}_{-0.45}$	⋯	⋯	$0.18^{+0.12}_{-0.09}$
Lorentzian 5	ν (Hz)	⋯	⋯	$1.40^{+2.48}_{-1.40}$	⋯	$0.98^{+0.32}_{-0.97}$
	Δ (Hz)	⋯	⋯	$6.61^{+2.45}_{1.59}$	⋯	$1.85^{+2.21}_{-0.84}$
	norm (10^{-3})	⋯	⋯	$1.27^{+0.32}_{-0.29}$	⋯	$0.83^{+0.60}_{-0.42}$
power law	α	⋯	⋯	⋯	$0.96^{+0.31}_{-0.20}$	⋯
	norm (10^{-5})	⋯	⋯	⋯	$2.84^{+1.36}_{-1.45}$	⋯
	chi2/dof	52/57	48/57	85/60	61/60	72/54

harmonic were also observed at ∼3.58 and ∼15.7 Hz respectively but the Q-value for subharmonic is less than 2 and the significance level for harmonic is less than 3.0σ. There is no QPO observed in Seg-3 and Seg-4.

To check the energy dependence of QPOs, we extracted the lightcurve in three different energy bands: 1–2 keV, 2–4 keV and 4–10 keV. We calculated the PDS in each energy range for Seg-1, Seg-2 and Seg-5. Figure 4 shows the PDS in energy ranges 1–2 keV, 2–4 keV and 4–10 keV for Seg-1, Seg-2 and Seg-5. In the soft energy band (1–2 keV), no QPO was observed for all segments. In energy band 2–4 keV, QPO was observed for Seg-1 and Seg-2 but no QPO was observed for Seg-5. In the energy band 4–10 keV, QPO was observed for all three segments. No signature of QPO in the soft energy band refutes the origin of QPO being from the disk. Therefore, the QPOs might be the result of oscillations in the corona. We will discuss the possible origin of QPOs in further detail in the following section.

3.2. Simultaneous Fit of the Photon, rms and Phase-lag Spectrum

To advance further and extract a deeper understanding of the system, we estimated the frequency-dependent phase lag in the energy ranges 1.0–2.0 keV, 2.0–2.8 keV, 2.8–3.5 keV, 3.5–4.5 keV, 4.5–6.0 keV and 6.0–10.0 keV. The phase lag is calculated with reference energy band 1.0–10.0 keV. $\phi(\nu)$ is the phase of the cross-spectrum as a function of frequency (e.g., Nowak et al. 1999) and it is related to the time lags between the selected bands as $\tau(\nu) = \phi(\nu)/2\pi\nu$. The phase lag is calculated in the frequency range of FWHM/2 at QPO frequency. We further used these energy ranges to calculate the rms spectra at observed QPO frequencies. To calculate the rms, we fitted the power spectra in each energy range by fixing the frequency of Lorentzian as given in Table 2 for Seg-1 and Seg-2. For Seg-5, we calculated the rms in the energy range 1.0–3.5 keV, 3.5–4.5 keV, 4.5–6.0 keV and 6.0–10.0 keV. The error in rms was calculated at the 1σ level. The fractional rms at QPO frequency in each segment increased monotonically with energy. Bendat & Piersol (2011) derived the error formula for a single power spectrum and a single cross-spectrum. Ingram (2019) presented new error formulae for the rms spectrum and energy-dependent cross-spectrum to overcome the issue of overfitting due to formulae presented in Bendat & Piersol (2011). In this work, we used formulae derived by Ingram (2019) to calculate the rms spectrum and energy-dependent time/phase lag spectrum. The definition used by Nowak et al. (1999) and Ingram (2019) is that +ve lag corresponds to hard lags soft. So, in the current scenario, the +ve lag corresponds to the subject band lagging the reference band. For the number of realizations, $N > 500$, we used a bias term equal to zero as recommended by Ingram (2019). Here N is the product of the number of segments in an observation with the number of frequencies binned in the range. We simultaneously fitted the photon, rms and phase-lag spectra for Seg-1, Seg-2 and Seg-5 data sets while we fitted only the photon spectra for Seg-3 and Seg-4 using the model `phabs*(diskbb+nthcomp)+dilution*vkompthdk` within the software package XSPEC V12.13.0c. The dilution

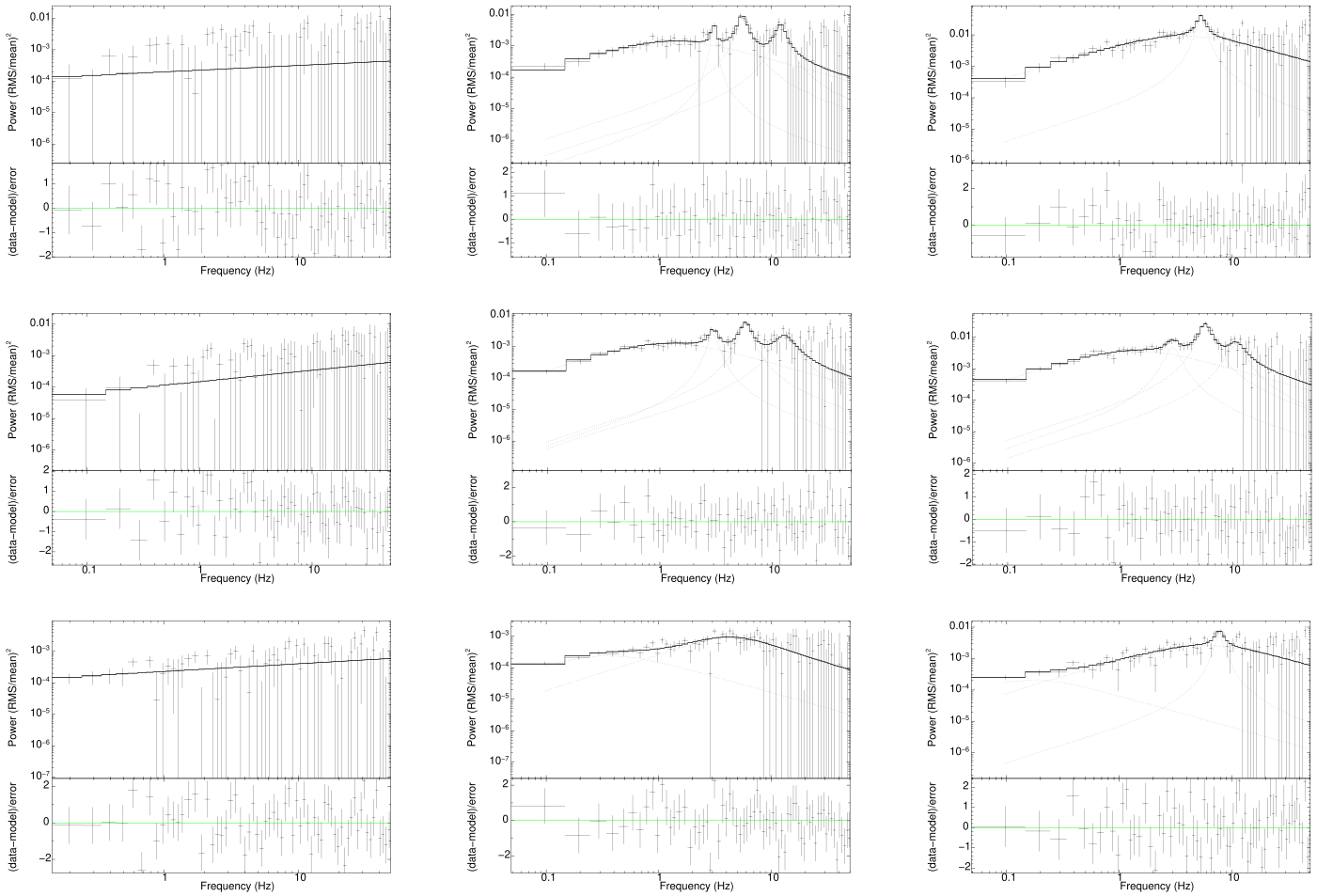

Figure 4. The PDS of Seg-1 (upper panel), Seg-2 (middle panel) and Seg-5 (lower panel) in energy range 1–2 keV (left panel), 2–4 keV (middle panel) and 4–10 keV (right panel).

parameter is defined as

$$\text{dilution} = \frac{\text{flux(nthcomp)}}{\text{flux(diskbb + nthcomp)}}.$$

In this model, the soft photons are supplied to the corona from the accretion disk (diskbb). Soft photons are inverse-Compton scattered by the hot electrons in the corona (nthcomp). The scattered photons finally escape the corona with higher energy forming the spectrum of the source. In this model, QPO is considered as a small oscillation of the source spectrum around the time-averaged spectrum. This model can generate both hard and soft lag in the time variation of the observed photon flux. `Phabs` describes the photoelectric absorption of X-rays. Even though `vkompth` has the provision to take multiple coronae, in our analysis we used only one corona. We fixed *kTe* of the nthcomp at 50 keV. An edge at ∼1.85 keV for Seg-3, Seg-4 and Seg-5 was used to account for the residuals observed possibly due to instrumental effects. The `vkompth` model contains the seed photon temperature, the electron temperature, the power law photon index, the size of the corona, the feedback fraction and the variation of the external heating rate. In simultaneous fitting, a `dilution` component was used for the rms spectrum to take care of the dilution effects due to disk. We tied the *kTe* and gamma of `vkompthdk` with *kTe* and gamma of nthcomp. The fitted parameters are given in the Table 3. Type-B QPO was not observed for Seg-3 and Seg-4. The PDS and energy spectrum for Seg-3 and Seg-4 are shown in Figure 5. Type-B QPO was observed for Seg-1, Seg-2 and Seg-5. For Seg-1, we obtained a corona size of ∼1705 km, with the feedback fraction of 10%. The seed photon source temperature of the corona was found to be $kT_s = 0.861^{+0.853}_{-0.159}$ keV. This is higher than the temperature of the inner disk, $kT_{\rm in} = 0.72 \pm 0.02$. The variation of the external parameter is found to be $\delta\dot{H}_{\rm ext} = 0.25^{+0.32}_{-0.07}$. For Seg-2, we obtained a corona size of ∼3926 km, with the feedback fraction of 9.4%. The seed photon source temperature of the corona was found to be $kT_s = 0.517^{+0.138}_{-0.137}$ keV. This is lower than the temperature of

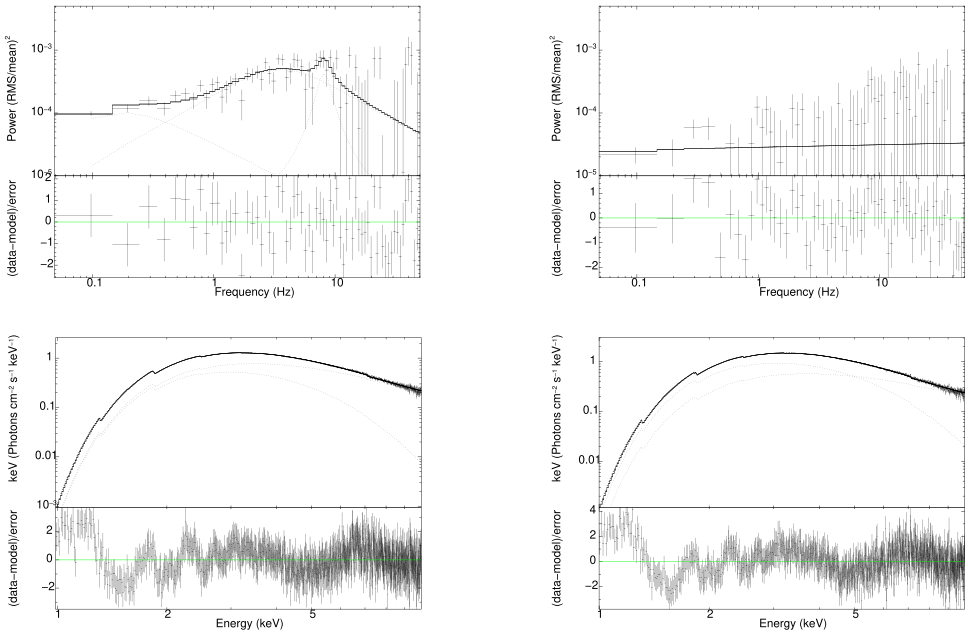

Figure 5. The PDS and energy spectrum of Seg-4 (left panel) and Seg-5 (right panel). Type-B QPO was not observed during these segments.

Table 3
The Simultaneous Fitting of the Photon, rms and Phase Lag Parameters for Seg-1, Seg-2 and Seg-5.

Component	Parameter	Seg-1	Seg-2	Seg-3	Seg-4	Seg-5
Phabs	$N_{\rm H}(\times 10^{22}$ cm$^{-2})$	$3.14^{+0.01}_{-0.01}$	$3.13^{+0.01}_{-0.01}$	$3.24^{+0.01}_{-0.01}$	$3.28^{+0.01}_{-0.01}$	$3.21^{+0.01}_{-0.01}$
diskbb	$kT_{\rm in}$	$0.72^{+0.02}_{-0.02}$	$0.77^{+0.02}_{-0.02}$	$1.04^{+0.01}_{-0.01}$	$1.11^{+0.01}_{-0.01}$	$0.92^{+0.01}_{-0.01}$
	$N_{\rm dbb}$	260^{+34}_{-42}	267^{+23}_{-27}	343^{+13}_{-14}	465^{+8}_{-8}	367^{+14}_{-15}
nthcomp	Γ	$2.54^{+0.03}_{-0.03}$	$2.61^{+0.02}_{-0.03}$	$2.82^{+0.06}_{-0.06}$	$2.46^{+0.09}_{-0.09}$	$2.80^{+0.03}_{-0.03}$
	norm	$1.62^{+0.12}_{-0.11}$	$1.75^{+0.10}_{-0.09}$	$1.70^{+0.12}_{-0.12}$	$1.10^{+0.11}_{-0.11}$	$1.92^{+0.11}_{-0.10}$
vkompthdk	KTs(keV)	$0.861^{+0.853}_{-0.159}$	$0.517^{+0.138}_{-0.137}$	...	...	$0.332^{+0.133}_{-0.105}$
	L (km)	1705^{+3402}_{-1310}	3926^{+4347}_{-2368}	...	...	7739^{+8437}_{-4438}
	η	$0.10^{+0.06}_{-0.06}$	$0.094^{+0.155}_{-0.075}$	...	...	$0.55^{*}_{-0.42}$
	$\delta\dot{H}_{\rm ext}$	$0.25^{+0.32}_{-0.07}$	$0.15^{+0.07}_{-0.04}$	...	...	$0.075^{+0.095}_{-0.034}$
	$F_{\rm Total}(\times 10^{-9})$	9.09 ± 0.01	10.54 ± 0.01	17.54 ± 0.02	20.16 ± 0.01	15.21 ± 0.01
	$F_{\rm diskbb}(\times 10^{-9})$	0.90 ± 0.01	1.27 ± 0.01	6.44 ± 0.02	11.65 ± 0.01	3.99 ± 0.01
	$F_{\rm nthcomp}(\times 10^{-9})$	8.19 ± 0.01	9.27 ± 0.01	11.10 ± 0.02	8.51 ± 0.01	11.22 ± 0.01
	$\frac{F_{\rm diskbb}}{F_{\rm Total}}$	0.10	0.12	0.37	0.58	0.26
	χ^2/dof	940/867	960/901	970/893	1145/893	967/897

Note. For Seg-3 and Seg-4, the Spectral Fitting Parameters are given. Here, $n_{\rm H}$: equivalent neutral hydrogen column density, $kT_{\rm in}$: inner disk temperature, $N_{\rm dbb}$: normalization of multicolor disk model diskbb, Γ: asymptotic power-law index of the Comptonized photon distribution, norm: normalization of nthcomp model, $kT_{\rm s}$: seed photon temperature of vkompthdk, L: size of the corona, η: feed fraction, $\delta\dot{H}_{\rm ext}$: variation of the external heating rate. The confidence ranges for the error bars are 68% CI. F_{Total}: total unabsorbed photon flux in the energy range 1.0–10.0 keV, $F_{\rm diskbb}$: photon flux from a thin accretion disk around a BH and $F_{\rm nthcomp}$: photon flux due to the Comptonized component. The units of flux are erg cm^{-2} s^{-1}

the inner disk, $kT_{\rm in} = 0.77 \pm 0.02$. The variation of the external parameter is found to be $\delta\dot{H}_{\rm ext} = 0.15^{+0.07}_{-0.04}$. For Seg-5, we obtained a corona size of ∼7739 km, with the feedback fraction of 56%. The seed photon source temperature of the corona was found to be $kT_s = 0.332^{+0.133}_{-0.105}$ keV. This is lower than the temperature of the inner disk, $kT_{\rm in} = 0.92 \pm 0.01$. The variation of the external parameter is found to be $\delta\dot{H}_{\rm ext} = 0.075^{+0.095}_{-0.034}$. The simultaneous fittings of the photon, rms and lag spectra for Seg-1, Seg-2, and Seg-5 are shown in Figure 6, Figure 7 and Figure 8 respectively.

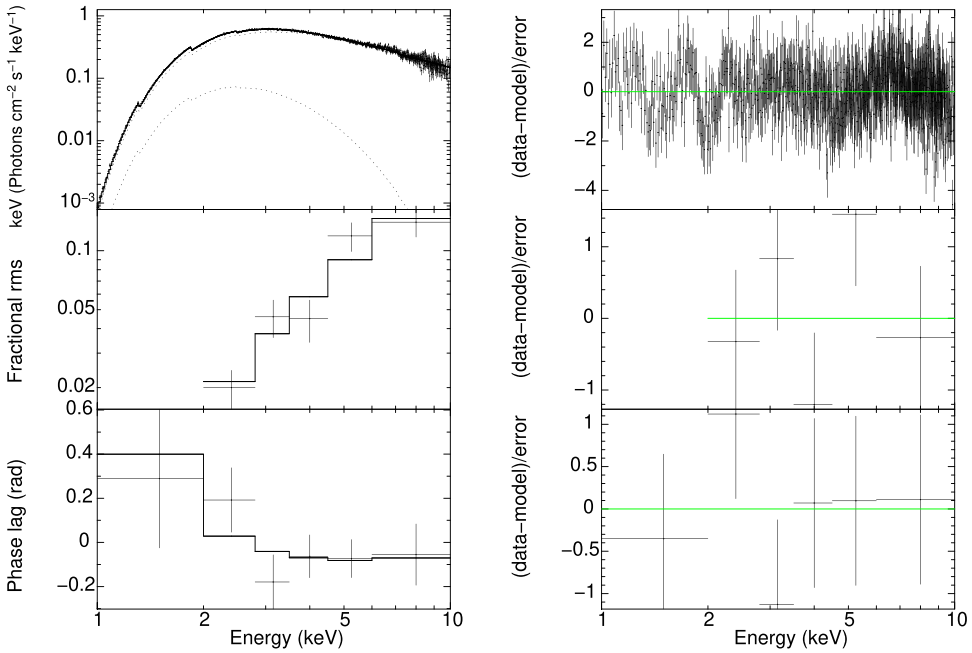

Figure 6. Simultaneous fitting of the photon, fractional rms and phase lag spectra for Seg-1. The rms and phase lag are calculated at ∼5.46 QPO frequency.

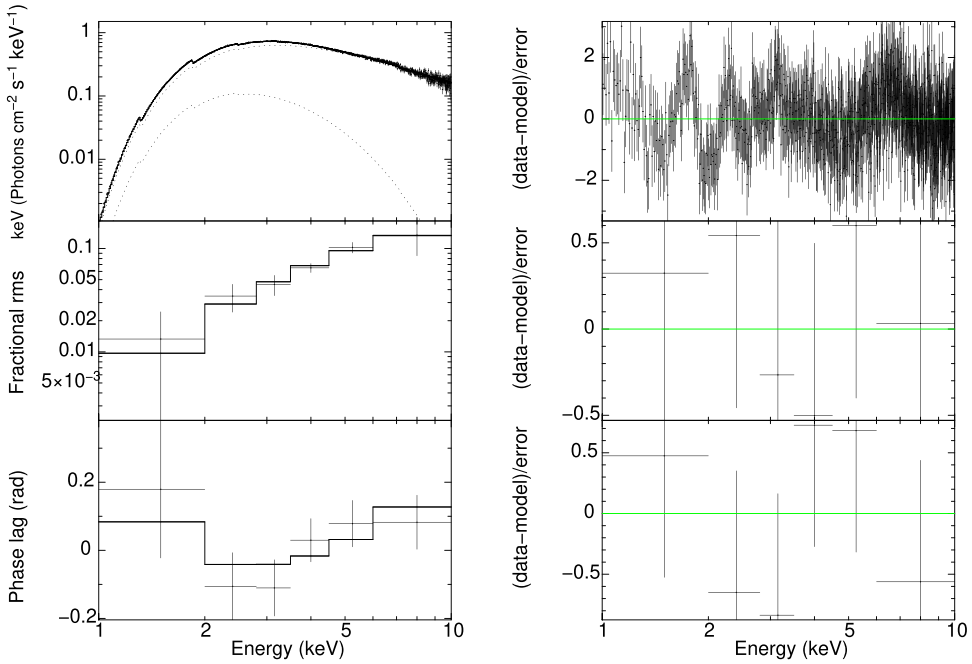

Figure 7. Simultaneous fitting of the photon, fractional rms and phase lag spectra for Seg-2. The rms and phase lag are calculated at ∼5.76 Hz QPO frequency.

Over the years, an enormous amount of research has been carried out to understand the behavior of the accretion process around astrophysical objects. The truncation disk model is a widely used model to explain the accretion process in moderately low accretion BH binary systems. In the canonical truncation disk, the outer region is the standard thin disk (Shakura & Sunyaev 1973) and the inner region consists of radiatively inefficient hot gas (Zdziarski & Gierliński 2004; McClintock & Remillard 2006; Done et al. 2007). The disk contribution to the total intrinsic photon flux was increased

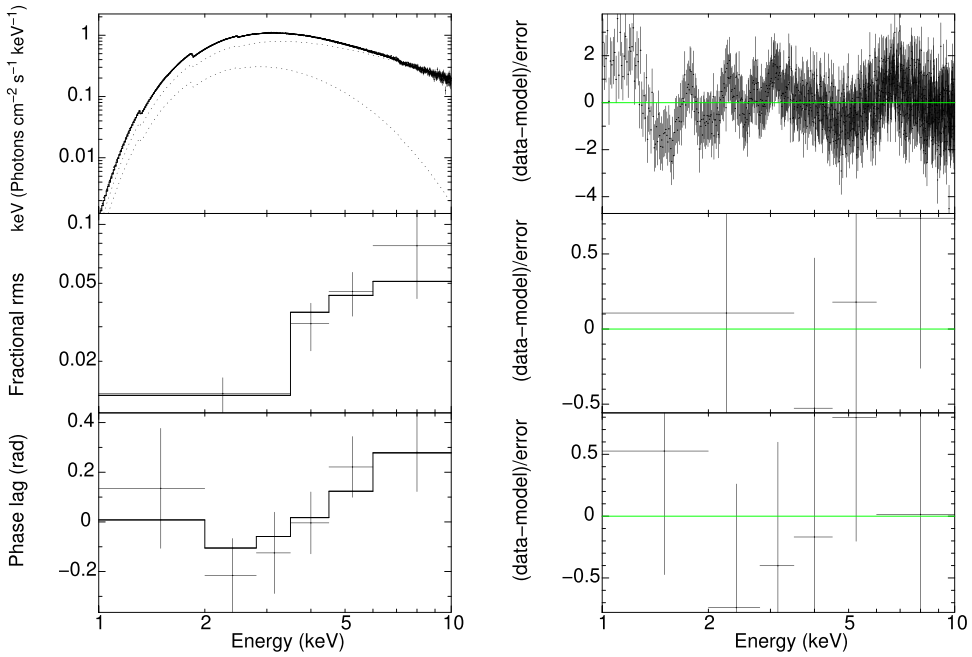

Figure 8. Simultaneous fitting of energy spectra, fractional rms and phase lag spectra for Seg-5. The rms and phase lag are calculated at ∼7.70 Hz QPO frequency.

from Seg-1 to Seg-4 and then decreased in Seg-5. The QPO was observed when the disk contribution was low or the corona contribution was more in the intrinsic photon flux.

The fundamental physical concept related to the appearance of SIMS and the associated type-B QPO is still unresolved. Using RXTE data, van den Eijnden et al. (2017) and Gao et al. (2017) noted that the lags of type-B QPOs are hard for low-inclination black hole binary (BHB) systems, while lags are either hard or soft for high inclination BHBs. In the literature on lags, there seems to be general agreement that inverse-Compton scattering of the soft photons in the corona produces hard lags (Miyamoto et al. 1988; Kylafis et al. 2008) while down-scattering of the hard photons in the disk produces soft lags (Uttley et al. 2014). Belloni et al. (2020) provided one of the earliest discussions of the positive lag below the 2 keV (0.7–2.0 keV) energy range. Their study of type-B QPO in MAXI J1348-630 found that the phase lags in 3–10 keV and 0.7–2.0 keV are positive with respect to reference band 2–3 keV. In their study, they discarded the possibility of the origin of type-B QPOs being due to the propagation of mass accretion rate fluctuations. Belloni et al. (2020) demonstrated that Comptonization of a flat seed photon spectrum between 2 and 3 keV with no emission at other energies can explain the positive lags of both low and high energies. This behavior will change for the more realistic seed photons (Peirano et al. 2023; Zhang et al. 2023a). The Comptonization model `vkompth` (Karpouzas et al. 2020; Bellavita et al. 2022) can account for the positive time lag at low energies and high energies. In Swift J1728.9-3613, we observed a "U-shaped" curve in the phase lag spectrum. This behavior indicates that the origin of type-B QPO in Swift J1728.9-3613 is related to the corona.

The `vkompth` has two different types based on the corona. `vkompthdk` is a model for one corona, where the corona is considered spherically symmetric. `vkdualdk` is a model for two coronae. It is considered a small corona and a large corona. Small corona are located near the BH and large corona can extend horizontally over the inner part of the accretion disk or extend vertically. This model is applied to investigate the geometry and disk-corona coupling. This model is used to explain the rms and phase lag of type-A QPO in MAXI J1348-630 (Zhang et al. 2023a), type-B QPO in MAXI J1348-630 (García et al. 2021; Bellavita et al. 2022), GX 339-4 (Peirano et al. 2023), MAXI J1535-571 (Zhang et al. 2023b), MAXI J1820+070 (Ma et al. 2023), GRO 1655-40 (Rout et al. 2023) and type-C QPO in MAXI J1820+070 (Ma et al. 2023), GRS 1915+105 (Karpouzas et al. 2021; García et al. 2022; Méndez et al. 2022), MAXI J1535-571 (Rawat et al. 2023), and GRO J1655-40 (Rout et al. 2023). For the type-B QPOs in Swift J1728.9-3613, we explained the rms and phase lag by one corona with varying size.

4. Summary and Conclusions

In a nutshell, NICER observed the BHXRB Swift J1728.9-3613 when the source was in the SIMS. A type-B QPO was observed during MJD 58512. During MJD 58513 the flux and hardness increased and type-B QPO disappeared. On MJD

58514, it showed a rapid transition to SIMS with the presence of type-B QPO. Xu et al. (2019) observed a rapid flux decrease of ∼45% in ∼40 s with turn-on of a QPO in BHXRB Swift J1658.2-4242 with NuSTAR, Swift and XMM-Newton. They suggest that the accretion disk instabilities triggered at a large disk radius cause the fast transition in spectral and timing properties of Swift J1658.2-4242. It can be noted that the type-B QPO was not observed in the soft energy band (1–2 keV) for any segment but it was present in the hard energy band 2–10 keV for seg-1, seg-2 and 4–10 keV for seg-5. The photons in 2–10 keV in the SIMS of BHXRB are produced by thermal Comptonization of the disk photons by the thermal electrons present in the corona. Therefore, the presence of QPO in 2–10 keV/4–10 keV possibly indicates that the QPO originated due to oscillations in the Comptonizing corona. The rms was found to be steadily increasing with energy for observed QPO.

In this work, we presented the study of spectral and timing properties of Swift J1728.9-3613 for MJD 58512, 58513 and 58514 using NICER observations. During the analyzed time, the source was in SIMS. The primary results are:-

1. We reported a type-B QPO at $\nu \sim 7.70$ Hz. This QPO was observed when there was a rapid decrease in the count rate from 1316 cts/sec to 990 cts/sec during MJD 58514.
2. Energy-dependent PDS reveals that observed QPO is not present in the low energy band, i.e., the 1–2 keV band, but it starts to appear at a higher energy range (after 2 keV for seg-1 and seg-2 but after 4 keV for seg-5). The rms and phase lag spectrum also indicate that observed QPO is modulated in the corona.
3. The rms and phase lag spectra are explained with the spherically symmetric corona. The size of the corona increased and the seed photon source temperature of the corona decreased with an increase in QPO frequency.

Acknowledgments

This work has made use of public NICER data available at https://heasarc.gsfc.nasa.gov/FTP/nicer/data/obs/ and the software provided by the High Energy Astrophysics Science Archive Research Center (HEASARC) available at https://heasarc.gsfc.nasa.gov/docs/software/lheasoft/. The time-dependent Comptonization model is available at the GitHub repositories https://github.com/candebellavita/vkompth. The author thanks Dr. Adam Ingram for help in calculating the time lag, Prof. Mariano Mendez for help in the `vkompthdk` model and the anonymous reviewer for their useful comments which improved the quality of the work.

ORCID iDs

Raj Kumar https://orcid.org/0000-0003-3469-9895

References

Balakrishnan, M., Draghis, P. A., Miller, J. M., et al. 2023, ApJ, 947, 38
Barthelmy, S. D., D'Ai, A., D'Elia, V., et al. 2019, ATel, 12436, 1
Bellavita, C., García, F., Méndez, M., & Karpouzas, K. 2022, MNRAS, 515, 2099
Belloni, T., Homan, J., Casella, P., et al. 2005, A&A, 440, 207
Belloni, T., Psaltis, D., & van der Klis, M. 2002, ApJ, 572, 392
Belloni, T. M. 2010, in Lecture Notes in Physics, Vol. 794 ed. T. Belloni (Berlin: Springer), 53
Belloni, T. M., & Motta, S. E. 2016, in Astrophysics of Black Holes: from Fundamental Aspects to Latest Developments, ed. C. Bambi (Berlin: Springer), 61
Belloni, T. M., Motta, S. E., & Muñoz-Darias, T. 2011, BASI, 39, 409
Belloni, T. M., Zhang, L., Kylafis, N. D., Reig, P., & Altamirano, D. 2020, MNRAS, 496, 4366
Bendat, J., & Piersol, A. 2011, Random Data: Analysis and Measurement Procedures (New York: Wiley)
Casella, P., Belloni, T., & Stella, L. 2005, ApJ, 629, 403
De Marco, B., Motta, S. E., & Belloni, T. M. 2022, in Handbook of X-ray and Gamma-ray Astrophysics, ed. C. Bambi & A. Santangelo (Singapore: Springer), 58
Done, C., Gierliński, M., & Kubota, A. 2007, A&ARv, 15, 1
Draghis, P. A., Balakrishnan, M., Miller, J. M., et al. 2023, ApJ, 947, 39
Enoto, T., Altamirano, D., Bult, P. M., et al. 2019, ATel, 12455, 1
Gao, H. Q., Zhang, L., Chen, Y., et al. 2017, MNRAS, 466, 564
García, F., Karpouzas, K., Méndez, M., et al. 2022, MNRAS, 513, 4196
García, F., Méndez, M., Karpouzas, K., et al. 2021, MNRAS, 501, 3173
Gendreau, K. C., Arzoumanian, Z., Adkins, P. W., et al. 2016, Proc. SPIE, 9905, 99051H
Gilfanov, M. 2010, in Lecture Notes in Physics, ed. T. Belloni, Vol. 794 (Berlin: Springer), 17
Heiland, S. R., Chatterjee, A., Safi-Harb, S., Jana, A., & Heyl, J. 2023, MNRAS, 524, 3834
Homan, J., & Belloni, T. 2005, Ap&SS, 300, 107
Ingram, A. 2019, MNRAS, 489, 3927
Joinet, A., Kalemci, E., & Senziani, F. 2008, ApJ, 679, 655
Karpouzas, K., Méndez, M., García, F., et al. 2021, MNRAS, 503, 5522
Karpouzas, K., Méndez, M., Ribeiro, E. M., et al. 2020, MNRAS, 492, 1399
Kylafis, N. D., Papadakis, I. E., Reig, P., Giannios, D., & Pooley, G. G. 2008, A&A, 489, 481
Ma, X., Zhang, L., Tao, L., et al. 2023, ApJ, 948, 116
McClintock, J. E., & Remillard, R. A. 2006, Compact Stellar X-ray Sources, Vol. 39 (Cambridge: Cambridge University Press), 157
Méndez, M., Karpouzas, K., García, F., et al. 2022, NatAs, 6, 577
Miyamoto, S., Kimura, K., Kitamoto, S., Dotani, T., & Ebisawa, K. 1991, ApJ, 383, 784
Miyamoto, S., Kitamoto, S., Mitsuda, K., & Dotani, T. 1988, Natur, 336, 450
Motta, S., Belloni, T., & Homan, J. 2009, MNRAS, 400, 1603
Motta, S., Muñoz-Darias, T., Casella, P., Belloni, T., & Homan, J. 2011, MNRAS, 418, 2292
Motta, S. E. 2016, AN, 337, 398
Nowak, M. A., Vaughan, B. A., Wilms, J., Dove, J. B., & Begelman, M. C. 1999, ApJ, 510, 874
Peirano, V., Méndez, M., García, F., & Belloni, T. 2023, MNRAS, 519, 1336
Rawat, D., Méndez, M., García, F., et al. 2023, MNRAS, 520, 113
Remillard, R. A., & McClintock, J. E. 2006, ARA&A, 44, 49
Rout, S. K., Méndez, M., & García, F. 2023, MNRAS, 525, 221
Saha, D., Mandal, M., & Pal, S. 2023, MNRAS, 519, 519
Shakura, N. I., & Sunyaev, R. A. 1973, A&A, 24, 337
Uttley, P., Cackett, E. M., Fabian, A. C., Kara, E., & Wilkins, D. R. 2014, A&ARv, 22, 72
van den Eijnden, J., Ingram, A., Uttley, P., et al. 2017, MNRAS, 464, 2643
Wijnands, R., & van der Klis, M. 1999, ApJ, 514, 939
Xu, Y., Harrison, F. A., Tomsick, J. A., et al. 2019, ApJ, 879, 93
Zdziarski, A. A., & Gierliński, M. 2004, PThPS, 155, 99
Zhang, L., Méndez, M., García, F., et al. 2023, MNRAS, 526, 3944
Zhang, Y., Méndez, M., García, F., et al. 2023b, MNRAS, 520, 5144